A Journal of the Gesellschaft Deutscher Chemiker

Angewandte International Edition Chemie

GDCh

www.angewandte.org

Accepted Article

Title: Reconfiguring the Hydrogen Networks of Aqueous Electrolyte to Stabilize Iron Hexacyanoferrate for High-Voltage Decoupled Cell

Authors: Zi-Long Xie, Yun-hai Zhu, Jia-Yi Du, Dong-Yue Yang, Ning Zhang, Qi-Qi Sun, Gang Huang, and Xin-bo Zhang

To be cited as: *Angew. Chem. Int. Ed.* **2024**, e202400916

Link to VoR: https://doi.org/10.1002/anie.202400916

WILEY VCH

10.1002/anie.202400916

WILEY-VCH

RESEARCH ARTICLE

Reconfiguring the Hydrogen Networks of Aqueous Electrolyte to Stabilize Iron Hexacyanoferrate for High-Voltage pH-Decoupled Cell

Zi-Long Xie[a,b+], Yunhai Zhu[c,+], Jia-Yi Du[a,b], Dong-Yue Yang[a,b], Ning Zhang[a,b], Qi-Qi Sun[a], Gang Huang[a,b,*], and Xin-Bo Zhang[a,b,*]

[a] Z.-L. Xie, J.-Y. Du, D.-Y. Yang, N. Zhang, Q.-Q. Sun, Prof. G. Huang, Prof. X.-B. Zhang
State Key Laboratory of Rare Earth Resource Utilization, Changchun Institute of Applied Chemistry, Chinese Academy of Sciences
Changchun 130022 (China)
E-mail: ghuang@ciac.ac.cn; xbzhang@ciac.ac.cn
[b] Z.-L. Xie, J.-Y. Du, D.-Y. Yang, N. Zhang, Prof. G. Huang, Prof. X.-B. Zhang
School of Applied Chemistry and Engineering, University of Science and Technology of China
Hefei 230026 (China)
[c] Prof. Y.-H. Zhu
State Key Laboratory of New Textile Materials and Advanced Processing Technologies, Wuhan Textile University
Wuhan 430200 (China)

Supporting information for this article is given via a link at the end of the document.

Abstract: Prussian blue analogs (PBAs) are promising insertion-type cathode materials for different types of aqueous batteries, capable of accommodating metal or non-metal ions. However, their practical application is hindered by their susceptibility to dissolution, which leads to a shortened lifespan. Herein, we have revealed that the dissolution of PBAs primarily originates from the locally elevated pH of electrolytes, which is caused by the proton co-insertion during discharge. To address this issue, the water-locking strategy has been implemented, which interrupts the generation and Grotthuss diffusion of protons by breaking the well-connected hydrogen bonding network in aqueous electrolytes. As a result, the hybrid electrolyte enables the iron hexacyanoferrate to endure over 1000 cycles at a 1 C rate and supports a high-voltage pH-decoupled cell with an average voltage of 1.95 V. These findings provide insights for mitigating the dissolution of electrode materials, thereby enhancing the viability and performance of aqueous batteries.

Introduction

Non-aqueous lithium-ion batteries (LIBs), known for their exceptional performance, currently stand as the preferred choice for portable electronics and electric vehicles[1]. However, the safety hazards of LIBs caused by the thermal runaways have raised great concern. This makes LIBs unpractical for grid-scale energy storage (GESS), which calls for batteries with cost-benefit and inherent safety[2,3]. Aqueous batteries, using aqueous electrolytes to replace hazardous, costly, and flammable organic electrolytes, have been regarded as promising candidates for GESS due to their advantages, including cheapness, high security, and environmentally benignity. To date, various aqueous battery prototypes using non-metallic or metallic charge carriers have been developed successively, which have aroused considerable attention with the increasing demand for renewable energy[4–12].

Aqueous batteries commonly consist of a metal anode and a cathode, which can be of insertion, conversion, or pseudocapacitive type. The electrolyte can be acidic, neutral, alkaline, or pH-decoupled electrolyte[13]. Compared with conversion-type and pseudocapacitive-type electrodes, the insertion-type materials experience no severe phase changes, allow for fast reaction kinetics, have a moderate capacity, and are suitable for long-term energy storage. Consequently, several insertion-type cathode materials have been investigated for application in aqueous batteries, including Prussian blue analogs (PBAs), manganese-based compounds, and vanadium-based compounds[12,14,15]. Among them, the PBAs stand out for their elevated electrode potential, versatile ion storage ability, cost efficiency, and facile synthesis. The PBAs typically have a chemical formula of $A_xM_2[M_1(CN)_6]_y{\cdot}zH_2O$ (A = energy storage carrier; M_1, M_2 = transition metal; $0 < x < 2$), wherein high-spin M_1N_6 and low-spin M_2C_6 octahedra are alternatively bridged by cyanide ligands to form a rigid three-dimensional framework. This open framework could facilitate rapid cation transfer along the <100> direction with minimal lattice strain, making PBAs suitable as ion-insertion cathodes. However, the PBAs suffer from severe capacity deterioration, whether accommodating the metal ions or non-metal ions, in the aqueous electrolytes. Explanations based on the Jahn-Teller effect or water-induced mechanism offer limited insights into the dissolution of Mn-free PBAs as well as the stability of PBAs soaked in acidic solutions[16–20]. The inherent mechanism underlying the capacity decay of PBAs remains elusive, and a mechanism-oriented strategy for electrode dissolution is needed [21–24].

Herein, we have unveiled that the capacity deterioration of PBAs is induced by their electrochemical dissolution. Combining the theoretical simulation with in-situ pH detection and electrochemical quartz crystal microbalance (EQCM), a locally elevated pH around the electrode surface accounts for the irreversible dissolution of PBAs, which is triggered by the proton insertion during discharge. To this end, we have introduced a water-locking strategy by using polyethylene glycol (PEG) to break the hydrogen network of the aqueous electrolyte, which curtails the Grotthuss diffusion of protons through the well-connected hydrogen network and then suppresses the proton insertion. As a result, the hybrid electrolyte allows for long-standing PBAs in aqueous electrolytes. It also supports a high-

10.1002/anie.202400916

voltage pH-decoupled cell, demonstrating the feasibility of this mechanism-oriented strategy in practical aqueous batteries.

Results and Discussion

Capacity Deterioration of PBAs Induced by the Electrochemical Dissolution

The iron hexacyanoferrate (FeHCF), a classic Prussian blue analog with dual redox centers contributing to its capacity, was selected as the primary specimen for investigation. The FeHCF was synthesized by a typical liquid-phase precipitation method, featuring a face-centered cubic structure with the space group $Fm\bar{3}m$ and a morphology of incomplete cubic nanoparticles (Figure 1a and Figure 1b)[25–27]. The uniform distribution of Fe, C, N, and O elements in the FeHCF was confirmed through the high-angle annular dark-field scanning transmission electron microscopy (HAADF-STEM) and energy-dispersive X-ray spectroscopy (EDX) mapping (Figure S1). Based on the thermogravimetric (TG) analysis and element analysis (Figure S2 and Table S1), the molecular formula of the as-prepared FeHCF is calculated to be $Fe[Fe(CN)_6]_{0.72}\cdot\square_{0.28}\cdot 3.6H_2O$, wherein the □ represents the $Fe(CN)_6$ vacancies. Notably, X-ray photoelectron spectroscopy (XPS) reveals that the low-spin Fe coordinated with C exists as a mixture of Fe^{2+} and Fe^{3+} in the pristine state of the material (Figure 1c)[26,28].

The electrochemical performance of FeHCF was verified in three-electrode cells, using 1 M KOTf solution, Ag/AgCl electrode, and active carbon electrode as the electrolyte, reference electrode, and counter electrode, respectively. In the potential range from −0.2 to 1 V (Vs. Ag/AgCl), the FeHCF exhibits an initial capacity of 102 mAh g^{-1} (Figure 1d). However, the FeHCF suffered from serious capacity deterioration, with a capacity retention of less than 50% after 100 cycles. This degradation worsened significantly at lower rates (Figure S3).

To explore the reason for the capacity deterioration, we first investigated the electrolyte compositions during cycling (Figure 1e). Elevated Fe concentration in the electrolyte upon cycling, as revealed by the inductively coupled plasma optical emission spectroscopy (ICP-OES) analysis, confirms the expected PBA dissolution. This result was further confirmed by the morphology evolution of the FeHCF electrode (Figure 1f-g and Figure S4). Scanning electron microscope (SEM) images highlight a transformation of FeHCF particles from nearly cubic to hollow structures after 100 cycles. X-ray powder diffraction (XRD) pattern of the post-cycling FeHCF confirms the identity of these hollow particles as FeHCF, along with reduced peak intensity (Figure 1h). Additionally, the ex-situ XRD analysis demonstrates only a minor structural change in the FeHCF, quantified as a volume change of just 1.69% (Figure S5), suggesting that there is minimal lattice distortion during the ion insertion process[9,10,22]. Collectively, these findings point towards electrode dissolution as the primary factor contributing to the capacity fading in FeHCF.

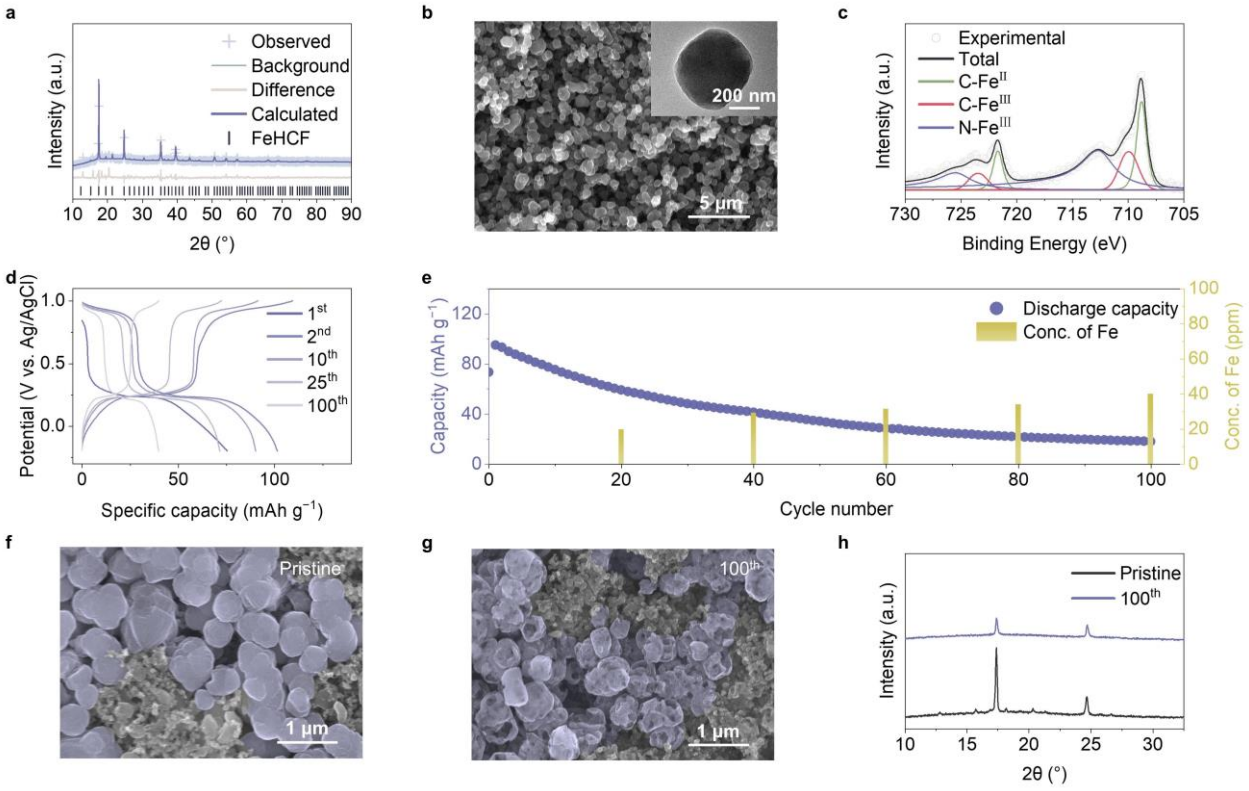

Figure 1. Charge/discharge profiles, structure, and morphology evolution of FeHCF. a, XRD refinement result of FeHCF. R_{wp} = 7.78%. b, SEM image of the synthesized FeHCF. The inset is the TEM image of FeHCF. c, XPS spectra of the Fe 2p for FeHCF. d, Charge/discharge profiles of FeHCF in the electrolyte of 1 M KOTf. e, In-situ detection of the Fe concentration during cycling. SEM images of the f, pristine FeHCF, and g, 100th cycled FeHCF, respectively. h, XRD patterns of pristine and post-cycling FeHCF.

10.1002/anie.202400916

RESEARCH ARTICLE

The Dissolution of FeHCF Caused by Locally Enriched OH^-

Considering that the dissolution of PBAs is more pronounced in aqueous electrolytes, we hypothesize that this process might be influenced by the pH of the electrolyte. To investigate this, the solubility of FeHCF in relation to the pH of the electrolyte was specifically examined. After being soaked in an alkaline electrolyte (1 M KOTf with 0.01 M KOH) for 12 hours, the original FeHCF particle morphology was broken and collapsed (Figure S6). In contrast, the electrodes exposed to the neutral and acidic electrolytes largely retained their pristine morphology. This is corroborated by the XRD analysis (Figure S7). The complete disappearance of FeHCF diffraction peaks suggests the conversion to amorphous $Fe(OH)_3$ induced by the long-time soak in the alkaline electrolyte[29,30,21]. It demonstrates that the PBA materials become unstable and dissolve rapidly, which leads to structural collapse due to the OH^- corrosion[31,32]. We then conducted in-situ monitoring measurement of the change in pH of the electrolyte during the charge-discharge process (Figure 2a) and found that the pH increased during the discharge process while the pH decreased during the charge process. The pH alternates cyclically alongside the charge and discharge process, which indicates that the proton insertion accompanies the potassium ion insertion in the FeHCF[33,34]. Notably, pH fluctuations are more responsive and dramatic at the electrode surface compared to the bulk electrolyte[35,36], indicating a localized impact of these changes. Based on these findings, we infer that the observed pH alteration is predominantly due to the proton insertion reactions. During the discharge process, proton insertion into FeHCF appears to stimulate water ionization, thereby elevating the pH and resulting in a localized increase in OH^-. This phenomenon leads to the dissolution of FeHCF. Conversely, during charging, protons are released from FeHCF, leading to a reduction in pH (Figure 2b).

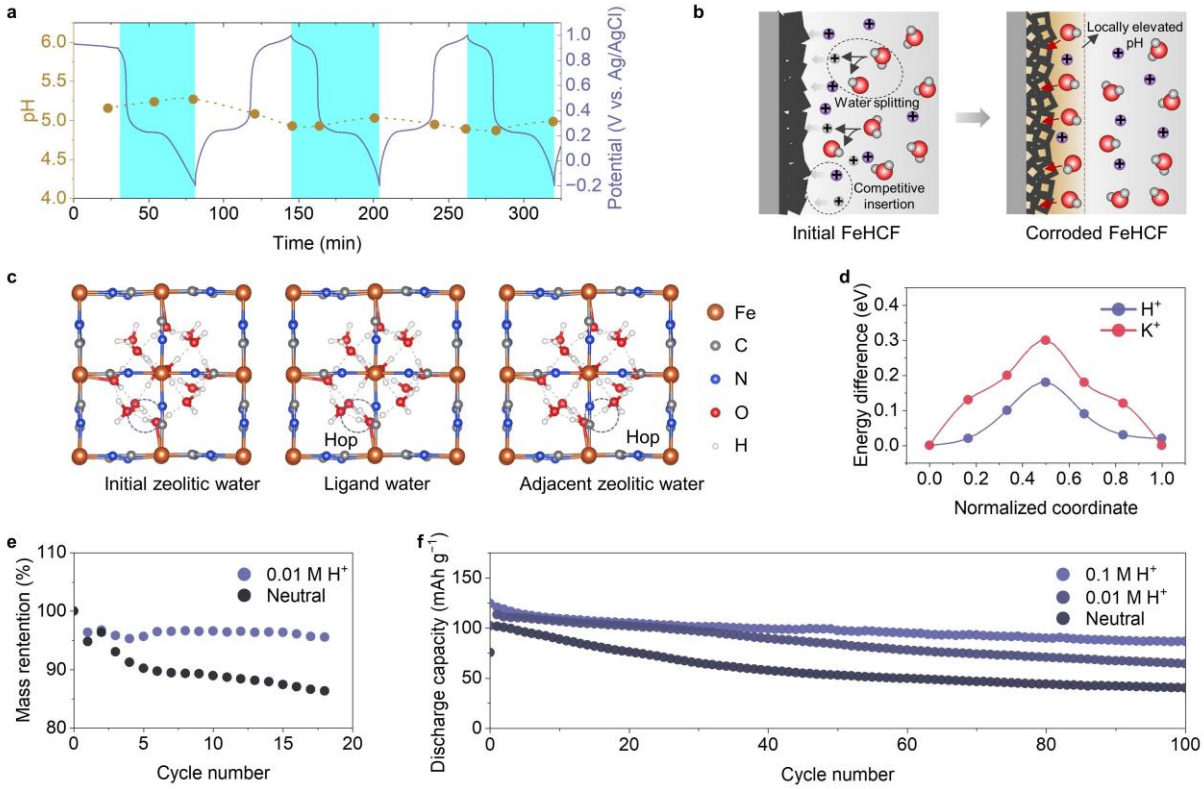

Figure 2. The proton involves an electrochemical process for FeHCF. a, In-situ pH detection of the bulk electrolyte during discharge and charge of the FeHCF. b, Scheme of the electrochemical dissolution of PBAs. c, The Grotthuss diffusion mechanism of the protons in FeHCF. d, Diffusion energy barriers of H^+ and K^+ in FeHCF. e, EQCM test for the mass retention of FeHCF with 0.005 M H_2SO_4 during cycling. f, Cycling performance of FeHCF in the electrolytes of 1 M KOTf with 0 M, 0.005 M, and 0.05 M H_2SO_4, respectively.

In our constructed battery system, there are two types of inserting ions: potassium ions and protons. These ions compete in the insertion reactions. We have confirmed the feasibility of proton insertion and its competitive advantage over the potassium ions. Besides the aqueous electrolyte environment, water molecules are inherently present within the crystal structure of PBAs in two forms: zeolitic water and coordination water. The zeolitic water is located at the A site, while the coordination water is situated at the vacancy defects, forming coordination interactions with the M^{2+} atoms.[37,38]. Notably, a variety of ions, especially protons, are capable of existing as hydrated ions within PBAs. This is especially pertinent when considering the protons' Grotthuss mechanism in water could greatly accelerate their transport rate[37,39]. Through the Climbing image nudged elastic band (CI-NEB), we investigated the insertion behavior of protons within the FeHCF. This process, transitioning from initial zeolitic water to ligand water and then to adjacent zeolitic water, was simplified into seven stages for computational feasibility (Figure 2c, Figure S8-S9). The proton transfer relies on the reorientation of the molecules along with the breaking and re-establishment of covalent O-H bonds. With a vacancy fraction of 1/4, the ligand water in the vacancy defect adequately connects all the zeolitic water at the A site, creating a hydrogen-bonding network for Grotthuss conduction of the proton[40]. The transferred proton

does not necessarily break the newly formed bonds. It strategically breaks the bond instead, which minimizes energy expenditure within the hydrogen bond network. This allows for efficient 'hopping' through the network, like a relay race. This mechanism shortens the overall proton migration distance and reduces the resistance of ion diffusion within the electrode[41,42]. The transfer of protons through the Grotthus mechanism has a 0.12 eV lower diffusion energy barrier than the conventional ion migration of potassium ions (Figure 2d), suggesting that the proton insertion is more kinetically favorable, leading to a faster diffusion rate in FeHCF. These findings validate the feasibility and capability of the proton insertion within the FeHCF.

To further verify the above conclusion, we pre-added a proton source to the electrolyte to avoid the localized OH^- enrichment caused by the dissociation of water, which, in theory, could inhibit the dissolution of FeHCF. We monitored the electrode mass change during the cycling of FeHCF under an acidic electrolyte by EQCM (Figure 2e). The FeHCF electrodes under acid electrolytes have higher mass retention in cyclic voltammetry scans. The results of the EQCM test illustrate that the electrode dissolution is significantly mitigated under acidic electrolytes. We also tested its cycling stability in different pH environments (Figure 2f). Adding a certain amount of acid to the electrolyte can significantly improve the cycling stability of FeHCF. But even in an acidic environment, the capacity decay is only slowed down to some extent rather than eliminated. The FeHCF grows into more angular particles after cycling in an acidity electrolyte (Figure S10). This Ostwald ripening phenomenon implies a possible cyclic shift in the dynamic equilibrium of material dissolution and regeneration[43–45].

The above experimental results demonstrate that the proton insertion in PBAs leads to increased local OH^- concentration, then the electrode material is corroded by the enriched OH^- on the electrode surface. This is the primary cause of the electrochemical dissolution of PBA in aqueous electrolytes. Although pre-adding a proton source can alleviate the capacity decay caused by PBA dissolution, it fundamentally cannot suppress the water-splitting reaction. As a result, while there is some improvement in cyclic performance, degradation still occurs. In addition to causing the dissolution, the proton co-insertion theoretically does not contribute to the capacity of the PBA material, which is primarily constrained by the valence change of its transition metal rather than the carrier species. Furthermore, in some aqueous battery systems, the production of layered double hydroxides on the electrode surface due to the consumption of protons by the hydrogen evolution reaction is known to diminish cycling stability[46,47]. Therefore, limiting the insertion of protons in PBAs would be a viable countermeasure to stabilize the electrode surface pH and inhibit material dissolution.

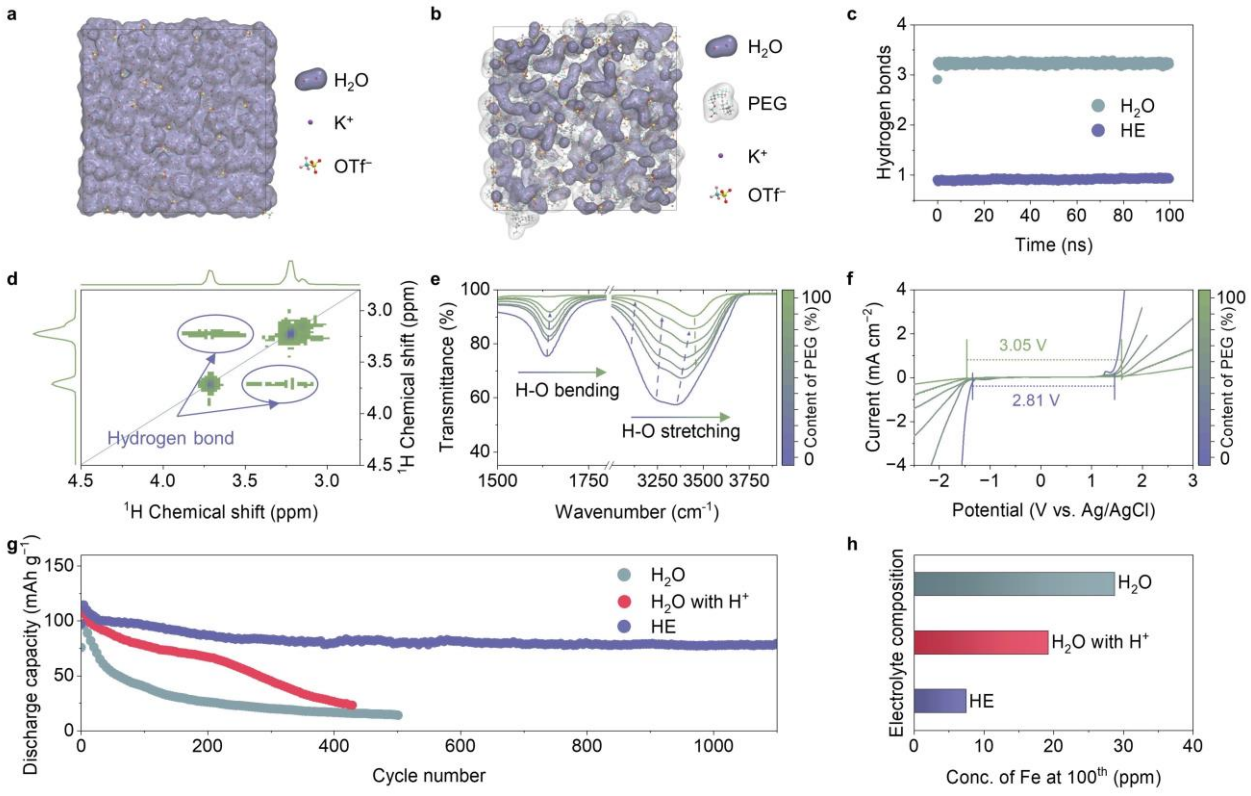

Figure 3. Breaking the hydrogen bonding network of aqueous electrolyte. MD snapshots of the electrolyte structures of a, 1 M KOTf in H_2O and b, HE (80 wt% PEG). c, Hydrogen-bond number of the electrolytes from MD. d, ^1H-^1H COSY of HE. e, FT-IR spectra, and f, LSV curves of HE with different ratios of PEG (wt%). g, Cycling performance of FeHCF in different electrolytes. h, Concentration of Fe element in the electrolytes after 100 cycles.

Reconfiguring the Hydrogen-Bonding Network to Suppress the Unexpected Proton Insertion

In neutral electrolytes, protons come from the dissociation of water. The hydrogen bonding between water molecules makes the O-H covalent bond easier to break, and the water molecules dissociate into protons and hydroxide ions in the form of hydrated ions[48,49]. Water is also a carrier of proton conduction. In addition to conventional directed diffusion, the Grotthuss conduction mechanism is also the dominant mode of proton conduction in

aqueous solutions[41,50]. Theoretically, introducing hydrogen-bond-coordinating molecules into the electrolyte could interrupt the hydrogen bond network of water and anchor water molecules, limiting their reorientation and mobility, and thereby inhibiting the generation and diffusion of protons. Considering that PEG could capture free water molecules through the hydrogen-bond interaction between its functional groups (terminal hydroxyl groups and interspersed ether linkages) and water, PEG was used as the electrolyte co-solvent to break the already formed hydrogen bonding network and then suppressed the proton transport[51–53].

Molecular dynamics (MD) simulations offer insights into the envisioned hydrogen bonding network of the electrolyte (Figure 3a-b). The snapshot shows the structure of electrolytes, where the PEG molecules are dispersed in the electrolyte. They anchor adjacent water molecules and form a new hydrogen bonding network where the hydrogen bond between water molecules is less continuous. This is quantitatively supported by a significant reduction of the water-water hydrogen bonds in the hybrid electrolyte (denoted as HE) (Figure 3c). Specifically, the number of hydrogen bonds per water molecule decreases to 0.9 in the HE, indicating difficulty in forming a well-connected network. We also examined the mean-squared displacement (MSD) of water molecules, finding a substantial decrease in the HE (Figure S11). This restriction in water molecule movement suggests that the PEG hinders their reorientation, a crucial aspect of the proton hopping mechanism within the Grotthuss model. This disruption contributes to slowing down the proton diffusion, supporting our expectation that the HE impedes proton transport. These results underscore the PEG's capacity to interrupt the hydrogen bonding network in water, substantially reducing its hydrogen bond count and thereby impeding proton diffusion.

We further investigated the structure of HE by nuclear magnetic resonance (NMR) spectroscopy, Fourier transform infrared spectroscopy (FT-IR), etc. The two-dimensional ^{1}H-^{1}H correlated spectroscopy (COSY) reveals the interaction between the different solvent molecules (Figure 3d). The interference signals in the circles represent the proton coupling between H_2O (peaks around 3.7 ppm) and PEG (peaks near 3.2 ppm), demonstrating the existence of an intermolecular hydrogen bonding network[54,55]. In the ^{1}H NMR (Figure S12), most of the peaks, especially the peak of H_2O, shifts downward compared to the pure solvents. This implies increased electron density due to the weakened interactions between water molecules[56]. In FTIR spectra (Figure 3e), as the content of PEG increases, the H-O bond stretching (around 3357 cm^{-1}) and bending vibration (about 1635 cm^{-1}) shift to higher wavenumbers. This indicates the strong interaction between PEG and H_2O. The weakening of hydrogen bonds between H_2O molecules means that PEG can interrupt the hydrogen bonding network of water. Moreover, due to the enhancement of water covalent bonding and diminished free water, the water decomposition reaction in the HE is effectively suppressed (Figure 3f). HE electrolytes have the non-flammable properties of water-based electrolytes and a better affinity to the electrodes (Figure S13-S14).

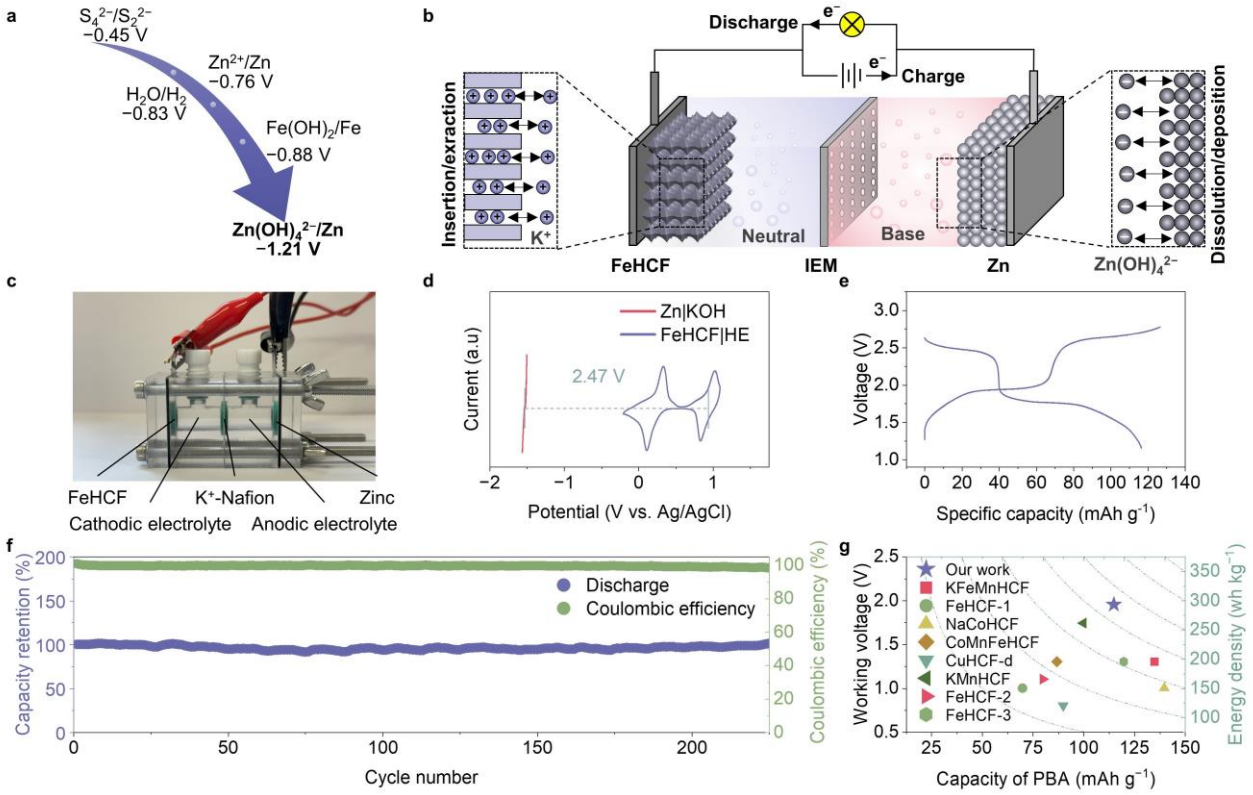

Figure 4. Performance of HE-based cells. a, Standard redox potentials for the anode candidates in neutral and alkaline electrolytes. b, Prototype of the designed pH-decoupled cell. c, Configuration of the decouple cell. d. CV curves of the selected anode and cathode. The redox pairs clearly give the voltage gap of the pH-decoupled cell. e, Charge/discharge profile of the selected anode and cathode. f, Cycling performance of the pH-decoupled cell at 1 C. g, Performance comparison of the decoupled cells with the reported works[9,26,27,57–61].

Subsequently, we evaluated the electrochemical performance of FeHCF in the HE. Although the addition of PEG inevitably decreases the electrolyte's ion conductivity, we prioritized the long-cycle stability and specific capacity when

optimizing the PEG content. The sample with 80% PEG exhibits the best overall performance (Figure S15-S17). As expected, the cycling stability of FeHCF in the HE is far superior to that in the control electrolyte (Figure 3g). This underscores the water-locking strategy as a fundamental solution to the material dissolution issue. After 100 cycles, the Fe content within the electrolyte was analyzed (Figure 3h). It reveals a marked reduction in concentration in HE, which is a notable improvement over the acidic electrolyte.

pH-Decoupled Cell with Water-Locking Strategy

To further demonstrate the adaptability of FeHCF in the HE, pH-decoupled cells that were capable of high-voltage operations were assembled. In view of the low potential of $Zn(OH)_4^{2-}/Zn$ redox pair (Figure 4a), we intended to construct high-voltage pH-decoupled cells by using FeHCF in HE as the cathode and Zn in an alkaline electrolyte as the anode. As shown in Figure 4b, this modular approach allows for integrating diverse electrode reactions via ion-exchange membranes (IEM). It significantly broadens the range of usable anode and cathode materials and their corresponding electrolytes[62–66]. To realize this novel prototype, we used a modular cell made of plexiglass (Figure 4c), which consists of FeHCF paired with a neutral HE electrolyte on the cathodic side and Zn metal coupled with an alkaline electrolyte on the anodic side, separated by a potassium ion exchange membrane. Utilizing this pH-decoupled battery design, the electrochemical window of the aqueous battery system is expanded, increasing the operating voltage and achieving higher energy output of the material.

Benefitting from the high voltage of PBA materials and pH-decoupled cell structure, the average discharge voltage of the pH-decoupled cell can reach 1.95 V, and the highest discharge plateau can reach nearly 2.5 V (Figure 4d-e, S18). Concurrently, the HE electrolytes effectively prevent hydroxide diffusion from the anodic side to the cathodic side since hydroxide may also diffuse through the hydrogen bonding network of water[67]. This ensures that the battery maintains stability over 450 hours (Figure 4f). Our work, within the published research employing non-concentrated electrolyte systems (Figure 4g), distinctly illustrates an echelon of energy density, fully harnessing the performance potential of the FeHCF material.

Conclusion

In summary, we have elucidated the electrochemical dissolution mechanism of PBAs in the aqueous electrolytes and designed a HE to solve this problem. The enriched OH^- on the electrode surface of PBA materials after H^+ insertion is the primary contributor to their dissolution. The HE has been designed to reconfigure the hydrogen bonding network of the electrolyte, proving the effectiveness in inhibiting the dissolution of electrode materials in aqueous electrolytes. Additionally, pH-decoupled cells have been constructed to not only combine the originally incompatible FeHCF with an alkaline anode but also break the limitation of the stability window of water to increase the operating voltage of the full cell. Considering that the electrode dissolution is a common but fatal problem in aqueous batteries, we believe that our strategy offers a viable and innovative solution to this pervasive issue.

Author Contributions

Z.-L.X. and Y.-H.Z. equally contributed to this work. Z.-L.X. focused on methodology, investigation, and the original draft writing. Y.-H.Z. handled conceptualization and manuscript editing. J.-Y.D., D.-Y. Y, N. Z., and Q.-Q. S. supported formal analysis, visualization, investigation, and validation, respectively. G. H. and X.-B. Z. oversaw supervision, and G. H. aided in editing, and X.-B. Z. contributed to conceptualization.

Acknowledgments

This work was financially supported by the National Key R&D Program of China (Grant 2022YFB2402200), National Natural Science Foundation of China (Grant 52271140, 52171194), Jilin Province Science and Technology Development Plan Funding Project (Grant YDZJ202301ZYTS545), National Natural Science Foundation of China Excellent Young Scientists (Overseas), and Youth Innovation Promotion Association CAS (Grant 2020230). The authors acknowledge Ceshigo for the technical support on theoretical calculations.

Keywords: Aqueous battery • Prussian blue analog • dissolution • Hydrogen bonds • Electrochemistry

[1] Z. Zhu, T. Jiang, M. Ali, Y. Meng, Y. Jin, Y. Cui, W. Chen, *Chem. Rev.* **2022**, *122*, 16610–16751.
[2] J. A. Jeevarajan, T. Joshi, M. Parhizi, T. Rauhala, D. Juarez-Robles, *ACS Energy Lett.* **2022**, *7*, 2725–2733.
[3] X. Feng, D. Ren, X. He, M. Ouyang, *Joule* **2020**, *4*, 743–770.
[4] F. Wang, O. Borodin, T. Gao, X. Fan, W. Sun, F. Han, A. Faraone, J. A. Dura, K. Xu, C. Wang, *Nat. Mater.* **2018**, *17*, 543–549.
[5] L. Cao, D. Li, E. Hu, J. Xu, T. Deng, L. Ma, Y. Wang, X.-Q. Yang, C. Wang, *J. Am. Chem. Soc.* **2020**, *142*, 21404–21409.
[6] L. Cao, D. Li, T. Pollard, T. Deng, B. Zhang, C. Yang, L. Chen, J. Vatamanu, E. Hu, M. J. Hourwitz, L. Ma, M. Ding, Q. Li, S. Hou, K. Gaskell, J. T. Fourkas, X.-Q. Yang, K. Xu, O. Borodin, C. Wang, *Nat. Nanotechnol.* **2021**, *16*, 902–910.
[7] J. Zheng, D. C. Bock, T. Tang, Q. Zhao, J. Yin, K. R. Tallman, G. Wheeler, X. Liu, Y. Deng, S. Jin, A. C. Marschilok, E. S. Takeuchi, K. J. Takeuchi, L. A. Archer, *Nat. Energy* **2021**, *6*, 398–406.
[8] T. Janoschka, N. Martin, U. Martin, C. Friebe, S. Morgenstern, H. Hiller, M. D. Hager, U. S. Schubert, *Nature* **2015**, *527*, 78–81.
[9] L. Jiang, Y. Lu, C. Zhao, L. Liu, J. Zhang, Q. Zhang, X. Shen, J. Zhao, X. Yu, H. Li, X. Huang, L. Chen, Y.-S. Hu, *Nat. Energy* **2019**, *4*, 495–503.
[10] J. Ge, L. Fan, A. M. Rao, J. Zhou, B. Lu, *Nat. Sustain.* **2021**, *5*, 225–234.
[11] Y. Yamada, K. Usui, K. Sodeyama, S. Ko, Y. Tateyama, A. Yamada, *Nat. Energy* **2016**, *1*, 16129.
[12] R. Lin, C. Ke, J. Chen, S. Liu, J. Wang, *Joule* **2022**, *6*, 399–417.
[13] Y. Zhu, Y. Cui, Z. Xie, Z. Zhuang, G. Huang, X. Zhang, *Nat. Rev. Chem.* **2022**, *6*, 505–517.
[14] J. Xu, X. Ji, J. Zhang, C. Yang, P. Wang, S. Liu, K. Ludwig, F. Chen, P. Kofinas, C. Wang, *Nat. Energy* **2022**, *7*, 186–193.
[15] Y. Liang, Y. Yao, *Nat. Rev. Mater.* **2022**, *8*, 109–122.
[16] Z. Zhu, Y. Meng, Y. Yin, Z. Liu, T. Jiang, Q. Peng, T. Yin, M. Li, W. Chen, *Energy Storage Mater.* **2021**, *42*, 464–469.
[17] R. Y. Wang, C. D. Wessells, R. A. Huggins, Y. Cui, *Nano Lett.* **2013**, *13*, 5748–5752.
[18] H. Yaghoobnejad Asl, A. Manthiram, *J. Am. Chem. Soc.* **2020**, *142*, 21122–21130.
[19] L. Zhang, L. Chen, X. Zhou, Z. Liu, *Adv. Energy Mater.* **2015**, *5*, 1400930.

[20] A. Indra, U. Paik, T. Song, *Angew. Chem. Int. Ed.* **2018**, *57*, 1241–1245.
[21] X. Lamprecht, F. Speck, P. Marzak, S. Cherevko, A. S. Bandarenka, *ACS Appl. Mater. Interfaces* **2022**, *14*, 3515–3525.
[22] L. Chen, W. Sun, K. Xu, Q. Dong, L. Zheng, J. Wang, D. Lu, Y. Shen, J. Zhang, F. Fu, H. Kong, J. Qin, H. Chen, *ACS Energy Lett.* **2022**, *7*, 1672–1678.
[23] S. Liu, J. He, D. Liu, M. Ye, Y. Zhang, Y. Qin, C. C. Li, *Energy Storage Mater.* **2022**, *49*, 93–101.
[24] W. Shu, J. Li, G. Zhang, J. Meng, X. Wang, L. Mai, *Nano-Micro Lett.* **2024**, *16*, 128.
[25] X. Wu, W. Deng, J. Qian, Y. Cao, X. Ai, H. Yang, *J. Mater. Chem. A* **2013**, *1*, 10130–10134.
[26] X. Wu, Y. Xu, H. Jiang, Z. Wei, J. J. Hong, A. S. Hernandez, F. Du, X. Ji, *ACS Appl. Energy Mater.* **2018**, *1*, 3077–3083.
[27] Q. Yang, F. Mo, Z. Liu, L. Ma, X. Li, D. Fang, S. Chen, S. Zhang, C. Zhi, *Adv. Mater.* **2019**, *31*, 1901521.
[28] X. Wu, M. Shao, C. Wu, J. Qian, Y. Cao, X. Ai, H. Yang, *ACS Appl. Mater. Interfaces* **2016**, *8*, 23706–23712.
[29] L. Zhang, H. B. Wu, X. W. (David) Lou, *J. Am. Chem. Soc.* **2013**, *135*, 10664–10672.
[30] W. Li, C. Han, G. Cheng, S. Chou, H. Liu, S. Dou, *Small* **2019**, *15*, 1900470.
[31] Z.-D. Gao, Y. Qu, T. Li, N. K. Shrestha, Y.-Y. Song, *Sci. Rep.* **2014**, *4*, 6891.
[32] J. C. L. Meeussen, M. G. Keizer, W. H. Van Riemsdijk, F. A. M. De Haan, *Environ. Sci. Technol.* **1992**, *26*, 1832–1838.
[33] H. Yang, W. Zhou, D. Chen, J. Liu, Z. Yuan, M. Lu, L. Shen, V. Shulga, W. Han, D. Chao, *Energy Environ. Sci.* **2022**, *15*, 1106–1118.
[34] W. Li, H. Xu, H. Zhang, F. Wei, L. Huang, S. Ke, J. Fu, C. Jing, J. Cheng, S. Liu, *Nat. Commun.* **2023**, *14*, 5235.
[35] Y. Yokoyama, T. Fukutsuka, K. Miyazaki, T. Abe, *J. Electrochem. Soc.* **2018**, *165*, A3299–A3303.
[36] S. Dresp, T. Ngo Thanh, M. Klingenhof, S. Brückner, P. Hauke, P. Strasser, *Energy Environ. Sci.* **2020**, *13*, 1725–1729.
[37] S. Ohkoshi, K. Nakagawa, K. Tomono, K. Imoto, Y. Tsunobuchi, H. Tokoro, *J. Am. Chem. Soc.* **2010**, *132*, 6620–6621.
[38] F. Ai, Z. Wang, N.-C. Lai, Q. Zou, Z. Liang, Y.-C. Lu, *Nat. Energy* **2022**, *7*, 417–426.
[39] L. Chen, H. Shao, X. Zhou, G. Liu, J. Jiang, Z. Liu, *Nat. Commun.* **2016**, *7*, 11982.
[40] A. Simonov, T. De Baerdemaeker, H. L. B. Boström, M. L. Ríos Gómez, H. J. Gray, D. Chernyshov, A. Bosak, H.-B. Bürgi, A. L. Goodwin, *Nature* **2020**, *578*, 256–260.
[41] S. Cukierman, *Biochim. Biophys. Acta BBA - Bioenerg.* **2006**, *1757*, 876–885.
[42] T. Ueki, M. Watanabe, *Macromolecules* **2008**, *41*, 3739–3749.
[43] W. L. Noorduin, E. Vlieg, R. M. Kellogg, B. Kaptein, *Angew. Chem. Int. Ed.* **2009**, *48*, 9600–9606.
[44] T. Van Westen, R. D. Groot, *Cryst. Growth Des.* **2018**, *18*, 4952–4962.
[45] Z. Cao, L. Wang, H. Zhang, X. Zhang, J. Liao, J. Dong, J. Shi, P. Zhuang, Y. Cao, M. Ye, J. Shen, P. M. Ajayan, *Adv. Funct. Mater.* **2020**, *30*, 2000472.
[46] J. Hao, B. Li, X. Li, X. Zeng, S. Zhang, F. Yang, S. Liu, D. Li, C. Wu, Z. Guo, *Adv. Mater.* **2020**, *32*, 2003021.
[47] X. Wang, Z. Zhang, S. Xiong, F. Tian, Z. Feng, Y. Jia, J. Feng, B. Xi, *Small* **2021**, *17*, 2100318.
[48] Z. Tie, S. Deng, H. Cao, M. Yao, Z. Niu, J. Chen, *Angew. Chem. Int. Ed.* **2022**, *61*, e202115180.
[49] S. Bi, Y. Zhang, S. Deng, Z. Tie, Z. Niu, *Angew. Chem. Int. Ed.* **2022**, *61*, e202200809.
[50] G. Liang, Y. Zhu, C. Han, *Matter* **2023**, *6*, 2503–2505.
[51] J. Xie, Z. Liang, Y.-C. Lu, *Nat. Mater.* **2020**, *19*, 1006–1011.
[52] S. Jin, J. Yin, X. Gao, A. Sharma, P. Chen, S. Hong, Q. Zhao, J. Zheng, Y. Deng, Y. L. Joo, L. A. Archer, *Nat. Commun.* **2022**, *13*, 2283.
[53] Q. Sun, T. Sun, J. Du, Z. Xie, D. Yang, G. Huang, H. Xie, X. Zhang, *Angew. Chem. Int. Ed.* **2023**, *62*, e202307365.
[54] A. J. Dingley, L. Nisius, F. Cordier, S. Grzesiek, *Nat. Protoc.* **2008**, *3*, 242–248.
[55] M. Ma, R. Huang, M. Ling, Y. Hu, H. Pan, *Interdiscip. Mater.* **2023**, *2*, 833–854.
[56] F. Ming, Y. Zhu, G. Huang, A.-H. Emwas, H. Liang, Y. Cui, H. N. Alshareef, *J. Am. Chem. Soc.* **2022**, *144*, 7160–7170.
[57] L. Ma, S. Chen, C. Long, X. Li, Y. Zhao, Z. Liu, Z. Huang, B. Dong, J. A. Zapien, C. Zhi, *Adv. Energy Mater.* **2019**, *9*, 1902446.
[58] X. Wu, J. J. Hong, W. Shin, L. Ma, T. Liu, X. Bi, Y. Yuan, Y. Qi, T. W. Surta, W. Huang, J. Neuefeind, T. Wu, P. A. Greaney, J. Lu, X. Ji, *Nat. Energy* **2019**, *4*, 123–130.
[59] W. Deng, Z. Li, Y. Ye, Z. Zhou, Y. Li, M. Zhang, X. Yuan, J. Hu, W. Zhao, Z. Huang, C. Li, H. Chen, J. Zheng, R. Li, *Adv. Energy Mater.* **2021**, *11*, 2003639.
[60] Z. Wang, Y. Xu, J. Peng, M. Ou, P. Wei, C. Fang, Q. Li, J. Huang, J. Han, Y. Huang, *Small* **2021**, *17*, 2101650.
[61] Y. Zeng, X. F. Lu, S. L. Zhang, D. Luan, S. Li, X. W. (David) Lou, *Angew. Chem. Int. Ed.* **2021**, *60*, 22189–22194.
[62] C. Zhong, B. Liu, J. Ding, X. Liu, Y. Zhong, Y. Li, C. Sun, X. Han, Y. Deng, N. Zhao, W. Hu, *Nat. Energy* **2020**, *5*, 440–449.
[63] Y. Cui, Y. Zhu, J. Du, Y. Zhang, K. Li, W. Liu, G. Huang, X. Zhang, *Joule* **2022**, *6*, 1617–1631.
[64] Y. Cui, Z. Zhuang, Z. Xie, R. Cao, Q. Hao, N. Zhang, W. Liu, Y. Zhu, G. Huang, *ACS Nano* **2022**, *16*, 20730–20738.
[65] Y. Xu, P. Cai, K. Chen, Y. Ding, L. Chen, W. Chen, Z. Wen, *Angew. Chem. Int. Ed.* **2020**, *59*, 23593–23597.
[66] D. Chao, C. Ye, F. Xie, W. Zhou, Q. Zhang, Q. Gu, K. Davey, L. Gu, S. Qiao, *Adv. Mater.* **2020**, *32*, 2001894.
[67] M. Chen, L. Zheng, B. Santra, H.-Y. Ko, R. A. DiStasio Jr, M. L. Klein, R. Car, X. Wu, *Nat. Chem.* **2018**, *10*, 413–419.

10.1002/anie.202400916

WILEY-VCH

SUPPORTING INFORMATION

Table of Contents

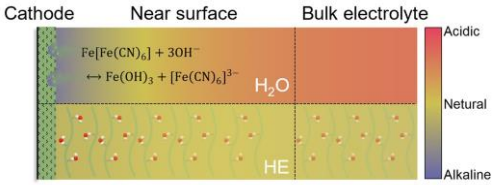

Proton insertion-induced local pH increase leads to PBA dissolution. Our strategy locks water molecules to disrupt the proton diffusion's hydrogen bond network, inhibit the proton insertion, and stabilize electrode pH, consequently ensuring stable PBA cathode cycling.